

Inci Ayranci¹
Suzanne M. Kresta¹
Jos J. Derksen^{1,2}

¹ University of Alberta, Chemical and Materials Engineering, Edmonton, Alberta, Canada.

² University of Aberdeen, School of Engineering, Aberdeen, Scotland, UK.

Research Article

Experiments and Simulations on Bidisperse Solids Suspension in a Mixing Tank

Experiments and simulations of a solids suspension process in a lab-scale stirred tank under turbulent conditions have been performed. Two impellers have been tested. The liquid-solid suspension consists of water and a mixture of glass and bronze particles. The simulations are Eulerian-Lagrangian with the liquid flow as the Eulerian part, being solved by means of a lattice-Boltzmann method combined with a large-eddy approach to turbulence modeling. Comparison with experimental visualizations indicates that the simulations are able to represent the start-up of the suspension process from a zero-velocity initial condition. Differences between experiment and simulation are observed near the bottom of the tank. The simulation data are used to highlight the collisional interaction between the two different types of solids, the role of baffles, and the effect of impeller type on the suspension process.

Keywords: Lattice-Boltzmann method, Mixing, Simulation, Solid-liquid suspension, Turbulence

Received: June 17, 2013; *revised:* August 15, 2013; *accepted:* August 16, 2013

DOI: 10.1002/ceat.201300409

1 Introduction

Liquid-solid suspensions are ubiquitous in nature and in technological systems. In engineering, solids transport (in pipelines) and solid-liquid contacting are amongst the more prominent applications. The goal of solid-liquid contacting is usually mass transfer, chemically reactive mass transfer in catalytic processes and hydrometallurgy, physical mass transfer in dissolution, and many crystallization applications. The purpose of liquid flow is to bring the solids in suspension so as to make available as much solid-liquid interfacial area as possible and to transport species through the liquid (toward and/or away from the solids).

In batch processes, the flow is usually generated by an impeller revolving in a tank under turbulent conditions with turbulence enhancing the transfer processes and assisting in the entrainment of solids in the liquid. Solids suspension in stirred tanks is a rich topic with a large number of experimental and computational research papers. Seminal experimental work is due to Zwietering [1] who studied minimal impeller speeds for solids suspension ("just-suspended speeds"). Zwietering's work has been assessed, refined, and extended by, among others, Nienow [2], Baldi et al. [3], and Davies [4]. Montante

et al. [5], and Dasari and Berson [6] combined experimental and computational (CFD) methods to study solids suspension in mixing tanks.

Recent work on solids suspension in stirred tanks deals with mixtures of different types of particles [7, 8] and addresses important questions about the interaction between the different particle types, i.e., direct interaction and interaction through the liquid. From a practical standpoint one wants to investigate if these interactions enhance or weaken the entrainment of solids in the liquid. As an example, it was shown experimentally by Ayranci and Kresta [8] that in one case the just-suspended speed decreases for hard to suspend particles in the presence of other particles.

CFD of solids suspension in mixing tanks has the potential of enhancing understanding and aiding process design. There is no universal approach for CFD of multiphase flow; the types of applications and computational cost largely dictate the methods to be used and the level of realism to be expected. Limiting ourselves to solid-liquid flows, the large-scale, turbulent, dense (high solids loading) flows benefit from Euler-Euler methods [5] that view liquid and solids as interpenetrating continua. They do not resolve individual solid particles and require empirical and theoretical input at multiple scales but are computationally affordable. Commercial CFD packages usually offer Euler-Euler capabilities. At the opposite side of the spectrum, small-scale systems and mesoscopic samples of larger systems allow for fully resolving the solid and liquid motion [9]. In between these two extremes, a broad range of methods exists with various levels of detail and applicability.

Correspondence: Prof. J. J. Derksen (jos@ualberta.ca), University of Alberta, Chemical and Materials Engineering, Edmonton, Alberta, T6G 2G6 Canada.

One of them, namely, Euler-Lagrange simulations with unresolved, colliding particles [10], has been applied in this paper.

The experimental facility as described in [8] has been employed for qualitative validation of our Eulerian-Lagrangian approach to simulating turbulent solid-liquid suspensions. Particles are tracked individually through a turbulent liquid flow field. The latter is obtained by solving the filtered Navier-Stokes equations by means of the lattice-Boltzmann method. The liquid motion on the sub-filter, i.e., subgrid scales is modeled through a simple Smagorinsky model with uniform coefficient $c_s = 0.1$ [11]. Since at this stage the number of solid particles one can deal with is limited for computational and modeling reasons, here it is reported on dilute suspensions (solids volume fractions of the order of 1 %) in a lab scale (tank diameter 24 cm) mixing tank. In future research we will go beyond dilute suspensions by introducing more refined ways for solid-liquid coupling [12].

The first objective of this paper is to directly compare experimental and numerical visualizations of the solids suspension process and thereby assess the level of realism of the simulations. Experiments were conducted showing the start-up of the process. By looking from the side, one can see how fast the solids are entrained in the liquid and transported through the tank volume. A view through the bottom reveals entrainment mechanisms in more detail [13]. These views are compared one-on-one with numerical visualizations. By studying the start-up of the process, not only steady operation is assessed but also the overall dynamics. The second objective is the assessment of the interactions between different particle types, i.e., bronze and glass, and their role in the solids suspension process. There is experimental evidence for the significance of such interactions [8]; its numerical confirmation will help in understanding and quantifying them. Finally, analysis of the simulation results provides insight in the way solids are circulated through the tank and how the circulation patterns, and thus the distribution of solids, can be affected by the impeller geometry and tank configuration.

The paper is subdivided in the following sections: First, the flow geometry, flow conditions, and particle properties are defined, as much as possible in terms of dimensionless numbers. Also the visualization experiments are briefly described there. The next section deals with the computational method and its major assumptions and simplifications. Simulation results are first discussed in the light of suspension start-up and experimental visualizations. Then patterns of liquid and solid motion through the tank are discussed. The final section reiterates the main findings.

2 Solid-Liquid Flow System Characteristics

The mixing tank and impeller geometries are given in Fig. 1. The cylindrical tank has an inner diameter of $T = 24$ cm and is filled with water (density $\rho = 1000$ kg m⁻³, viscosity $\nu = 1 \times 10^{-6}$ m² s⁻¹) and solids. The level of the free surface is

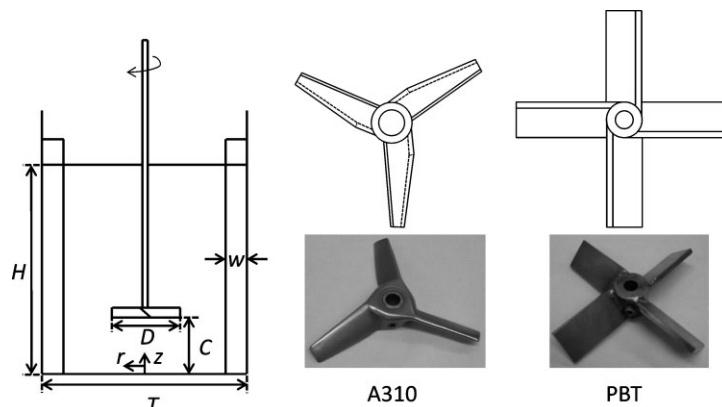


Figure 1. Schematic of tank geometry and impellers. Left: tank with $H = T$, $D = T/3$, $w = T/10$. Two off-bottom clearances ($C = 0.25T$ and $0.20T$) have been investigated. The origin of the r - z coordinate system is in the center on the bottom of the tank. Middle: Lightnin A310 impeller; right: pitched-blade turbine (PBT).

at $H = T$. Four baffles, equally spaced by 90°, are placed at the perimeter of the inner tank wall. The tank is optically accessible from the sides and from the bottom. Two types of impellers have been used: a Lightnin A310 impeller with diameter $D = T/3$ and a four-blade, 45°-pitched-blade turbine (PBT), also with $D = T/3$. The impellers are mounted on a shaft that enters the tank from the top. They rotate such that they pump in the downward direction; their angular velocity is denoted by N (rev s⁻¹).

The off-bottom clearance C has been set to two values: $C = 0.25T$ and $0.20T$. The Reynolds number that in addition to the geometry determines the liquid flow is defined as $Re \equiv ND^2/\nu$. Four flow cases have been studied and are summarized in Tab. 1. The Reynolds numbers are of the order of 10^5 ; strongly turbulent flow is expected. Reynolds number effects are investigated through variation of the impeller speed (viz. cases #3 and #4). The power numbers $Po \equiv P/(\rho N^3 D^5)$, with P the power inserted by the revolving impeller for the A310 and PBT are approximately 0.3 and 1.3, respectively [14], so that at the same impeller speed a much more energetic flow and stronger turbulence are expected for the PBT.

Table 1. Liquid flow characteristics.

Case #	Impeller	Clearance C/T	N [rev s ⁻¹]	v_{tip} [m s ⁻¹]	Re
1	A310	0.25	15	3.77	9.6×10^4
2	A310	0.20	15	3.77	9.6×10^4
3	PBT	0.25	15	3.77	9.6×10^4
4	PBT	0.25	10.8	2.71	7.0×10^4

The four cases all contain the same set of solid particles: 0.0128 kg bronze particles with density $\rho_{p,b} = 8860$ kg m⁻³ and diameters in the range $d_p = 150$ – 297 μ m (volume-based average diameter $d_{p,b} = 220$ μ m) and 0.250 kg glass beads (density $\rho_{p,b} = 2500$ kg m⁻³) with diameters in the range $d_p = 595$ – 841 μ m (volume-based average diameter $d_{p,g} = 720$ μ m). Both types of

particles are approximately spherical. Further details about the particles can be found in [8] (bronze denoted there as B, glass beads as LG in that paper).

Given their mass and density, the tank-average volume fractions are $\bar{\phi}_b = 1.3 \times 10^{-4}$ and $\bar{\phi}_g = 9.2 \times 10^{-3}$ for bronze and glass, respectively. The Stokes numbers, defined as $St \equiv \rho_p d_p^2 N / (18 \rho \nu)$, are 0.35 and 1.1 (based on $N = 15 \text{ rev s}^{-1}$) for bronze and glass, respectively. These values of order one imply that the response time of particles is of the order of the period of one impeller revolution and indicate that the particles are not flow followers (tracers) nor independent of the local flow conditions. The ratios of single particle settling velocities over the impeller tip speed $U_\infty / v_{\text{tip}}$ (again for $N = 15 \text{ rev s}^{-1}$) are 0.026 for bronze and 0.018 for glass. For determining U_∞ , the particles are assumed spherical with their volume-average diameter and the Schiller-Naumann drag correlation was applied [15] (see also [10]).

In summary, the suspension is dilute (overall solids volume fraction approximately 1%, overall mass fraction 2.5%), the flow is expected to be sufficiently strong to lift up at least a portion of the particles ($U_\infty / v_{\text{tip}} \approx 0.02$), and Stokes numbers are order one.

The startup of the solids suspension process has been visualized experimentally. The initial condition is a zero velocity field with all particles on the bottom of the tank. At time equals zero the impeller is switched on impulsively and the tank is filmed through the bottom and through the side at a rate of 30 frames per second and with a 640×480 pixels resolution. Filming is continued until steady state is reached. The simulations are processed such as to give a view similar to the experimental visualizations.

3 Modeling Approach

The simulation of the multiphase flow in the stirred tank has two main parts: an Eulerian description of the liquid flow and a Lagrangian description of the solids. As indicated in the introduction, liquid and solid are one-way coupled, i.e., the solids move around in the tank as a result of the liquid flow (hydrodynamic forces), gravity, and particle-particle collisions. The liquid, however, does not feel the presence of the particles. Given the, on average, low solids volume fraction (see above), this is a fair assumption. As will be seen, close to the bottom where solids concentrations are high compared to the average, one-way coupling might be too crude an approach.

The liquid flow is solved in a 3D time-dependent manner by means of the lattice-Boltzmann method (LBM) [16]. For this method, the tank volume is discretized by a uniform, cubic lattice with a resolution such that the tank diameter T spans 200 lattice spacings Δ ($T = 200\Delta$; and given $T = 24 \text{ cm}$, $\Delta = 1.2 \text{ mm}$). Discrete steps are taken in time of size $\Delta t = (2400N)^{-1}$, i.e., the impeller makes one revolution over 2400 time steps. Space and time resolution are insufficient to directly solve the Navier-Stokes equations for this turbulent flow. For direct simulations, a resolution is needed such that $\Delta \leq \pi \eta_K$ with η_K being the Kolmogorov length scale [17]. The latter can be estimated by means of the Reynolds number: $\eta_K / L = \text{Re}^{-3/4}$ with L a macroscopic length scale for which a rea-

sonable estimate is the impeller diameter D . With Re of order 10^5 , $\eta_K \approx 2 \times 10^{-4} D$ and thus $\Delta \approx 100 \eta_K$, so that small-scale eddies are not resolved by the grid. A Smagorinsky subgrid-scale model [11] is used to account for the influence of the small-scale turbulent motion on the resolved part of the flow field. The Smagorinsky model views the small eddies as purely diffusive with an eddy diffusivity (ν_e) that depends on the resolved deformation rate: $\nu_e = \lambda_{\text{mix}}^2 \sqrt{S^2}$ with $S^2 = \frac{1}{2} \left(\frac{\partial u_i}{\partial x_j} + \frac{\partial u_j}{\partial x_i} \right)^2$ (summation convention implied) and u_i the resolved liquid velocity. The mixing length is modelled as $\lambda_{\text{mix}} = c_s \Delta$. For the Smagorinsky constant a uniform value $c_s = 0.1$ is adopted [18]. Wall damping functions are not included; in mixing tank flows their impact is very limited [19]. The total viscosity $\nu + \nu_e$ is incorporated in the momentum equations that are solved with the LBM.

The no-slip conditions at the impeller blades moving through the fixed lattice is imposed by means of an immersed boundary method [20]. In this method, the impeller is represented by a collection of closely spaced points, i.e., some 16 000 in total with typical spacing 0.6Δ , on its surface. The interpolated liquid velocities at these points are forced to the same, and known, velocity of the impeller surface. A similar approach is used to force the liquid velocity to zero at the cylindrical tank wall and the baffles. The flat bottom has its no-slip character represented by a bounce-back boundary condition [16]; the top surface is assumed to be flat and has a free-slip boundary condition.

The approach sketched above has been used extensively for modeling turbulent [21] and transitional [22] stirred-tank flow. The method has been verified by means of grid refinement studies and validated by experimental data [21].

The solid particles in the tank feel the liquid through the drag force and the hydrostatic pressure, providing a buoyancy force on the particles. Only linear motion, not rotation, of the particles is considered. The particles are solid spheres with diameter d_p and density ρ_p . The equation of motion solved for each particle has the form:

$$\frac{dv_i}{dt} = g_i \frac{\rho_p - \rho}{\rho_p} + 18 \frac{\rho}{\rho_p} \frac{\nu}{d_p^2} f(\text{Re}_p) (u_i - v_i) \quad (1)$$

where v_i is the i -th component of the particle's velocity, g_i is the gravitational acceleration, and $f(\text{Re}_p) = \left(1 + 0.15 \text{Re}_p^{0.687} \right)$ is the Schiller-Naumann correction (see [10, 15]) to Stokes drag as a function of the particle Reynolds number $\text{Re}_p \equiv d_p \sqrt{(u_i - v_i)^2} / \nu$. Particle locations x_i satisfy $\frac{dx_i}{dt} = v_i$.

Eq. (1) is updated in a semi-implicit way:

$$v_i^{(k+1)} = v_i^{(k)} + \Delta t \left[g_i \frac{\rho_p - \rho}{\rho_p} + 18 \frac{\rho}{\rho_p} \frac{\nu}{d_p^2} f(\text{Re}_p^{(k)}) \left(u_i^{(k+1)} - v_i^{(k+1)} \right) \right] \quad (2)$$

with the upper index k the time step number. Eq. (2) indicates that the particle velocities are updated after the liquid velocity update $u_i^{(k+1)}$. The particle locations are updated in an Euler forward manner: $x_i^{(k+1)} = x_i^{(k)} + \Delta t v_i^{(k+1)}$. The time step for

the particle updates is the same as for the flow field. The resolved liquid velocities $u_i^{(k+1)}$ in Eq. (2) are linearly interpolated from the lattice to the particle location x_i . It is assumed that the particles do not feel the subgrid-scale velocities. This is justified given that the strength of the (estimated) subgrid-scale velocity fluctuations is much weaker than the resolved ones. With a similar resolution and Reynolds number, we earlier showed [10] that subgrid-scale velocity fluctuations are at least one order of magnitude smaller than their resolved counterparts.

Particles collide elastically and smoothly (restitution coefficient $e=1$, friction coefficient $\mu=0$) with one another, with the impeller, and with the tank wall including baffles. The hard-sphere collisions between particles are explicitly resolved with particle velocity and position updates within the time step in which the collision occurs. For reasons of computational efficiency, the number of particle-particle collisions is limited such that any given particle can only collide once per time step. This is a fair assumption for the dilute suspensions. The collision algorithm is due to Chen et al. [23]. All particles of the same type, i.e., bronze and glass, have the same diameter ($d_{p,b}=220\ \mu\text{m}$, $d_{p,g}=720\ \mu\text{m}$), respectively. The collision algorithm allows for collisions between unequal particles. The total number of particles is 775 109 with 260 772 bronze and 514 337 glass.

The way of dealing with the solid particles in this paper is simpler and as a result computationally more affordable compared to earlier simulations presented in [10]. Most importantly, rotation of particles and the associated Magnus lift force on the particles are not included and particle-to-liquid coupling is not considered. As discussed above, particle-particle collisions are included as these proved essential for realistically mimicking the suspension process, specifically in the lower regions of the tank [10]. The availability of experimental visualizations of the start-up of the suspension process is a qualitative way to assess to what extent the simplifications and schematizations in the simulations limit the level of realism of the simulations.

Despite some simplifications, the computational effort is still significant. On a single (2011 state-of-the art) CPU, a simulation typically advances three impeller revolutions per day. With runs spanning 100 revolutions, overall run times, therefore, need to be measured in weeks. A simulation occupies some 0.7 Gbyte of memory.

4 Results

4.1 Suspension Start-Up

The discussion of the results is started by showing the start-up of the suspension process for the four cases defined in Tab. 1. Figs. 2 and 3 present sequences of side views and bottom views, respectively, and compare experiments and simulations. Given the way particle-particle collisions and limitations on the local maximum solids volume fraction are dealt with, the simulation procedure does not allow starting with all particles lying on the bottom. For this reason, the start occurs with all particles randomly distributed and non-over-

lapping in a layer with thickness $0.175T$ directly above the bottom of the tank (in this layer $\phi \approx 0.06$). This makes a difference compared to the experiment in a few respects. The initial solids layer is thicker and more dilute, and more random in the simulations. In the experiment, the bronze particles tend to collect near the perimeter of the bottom, between the baffles and the moment the impeller is started they are preferentially concentrated there. This effect is apparent from the initial experimental frames in the bottom view (in Fig. 3). Another difference between simulation and experiment is that bronze and glass particles in the simulations have a uniform size for which their average sizes are taken: $d_{p,b}=220\ \mu\text{m}$ and $d_{p,g}=720\ \mu\text{m}$; in the experiment the particle size is distributed [8].

In the visualizations of the simulations it was tried to some extent to mimic the way the particles show in the experiment. In the experiment, the tank is viewed from the outside through the transparent side and bottom, respectively, the glass beads show as white/yellow, and the bronze particles as darker brown. In the simulations the same view is taken, i.e., a particle is observed as long as it is not obscured by another particle, a baffle, the impeller, or the shaft, with glass and bronze being yellow and black, respectively. The pixel size of the simulation frames in Figs. 2 and 3 is slightly larger than the bronze particle diameter, namely, 300 versus $220\ \mu\text{m}$. A bronze and a glass particle both show as one pixel in the simulation frames which is slightly different from the experiment where the bigger glass beads appear more pronounced compared to the smaller bronze particles.

The tank side views (Fig. 2) indicate that the time scales over which the solids suspension process evolves towards a steady state in experiment and simulation are approximately the same. In all cases there is no qualitatively significant difference between the snapshots at $tN=30$ and 40 and it is concluded that beyond $tN=40$ the process is dynamically steady. Seen from the side, differences between case #1 and #2 (A310 with $C/T=0.25$ and 0.20 , respectively) are marginal. Case #3 (PBT) starts up slightly faster than case #1 and #2. With the time measured in impeller revolutions as in Fig. 2, the solids cloud in case #4 rises quicker than in case #3. This is all related to the flow field that is generated by the two impellers and will be discussed later. The impact of the impeller speed is significant as can be concluded from comparing case #3 and #4. In steady state, case #4 ($N=10.8\ \text{rev s}^{-1}$) has a larger volume almost void of particles in the top region of the tank. Note that in Figs. 2 and 3 the time is scaled with the period of one impeller revolution so that the real time for the images of case #4 is larger than for the other cases.

Views through the bottom of the tank are given in Fig. 3. Even more pronounced than in Fig. 2, the difference in initial condition between experiment and simulation is evident. From the start, the particles in the experiment are segregated with the bronze particles mainly along the perimeter of the tank bottom. Except maybe for case #3, the flow generated by the impeller is not able to fully remove the bronze particles from this location. The bronze particles seem caught between the baffles; specifically in case #4 they pile up in front of the baffles. Note the counter clockwise rotation of the impeller in the views of Fig. 3.

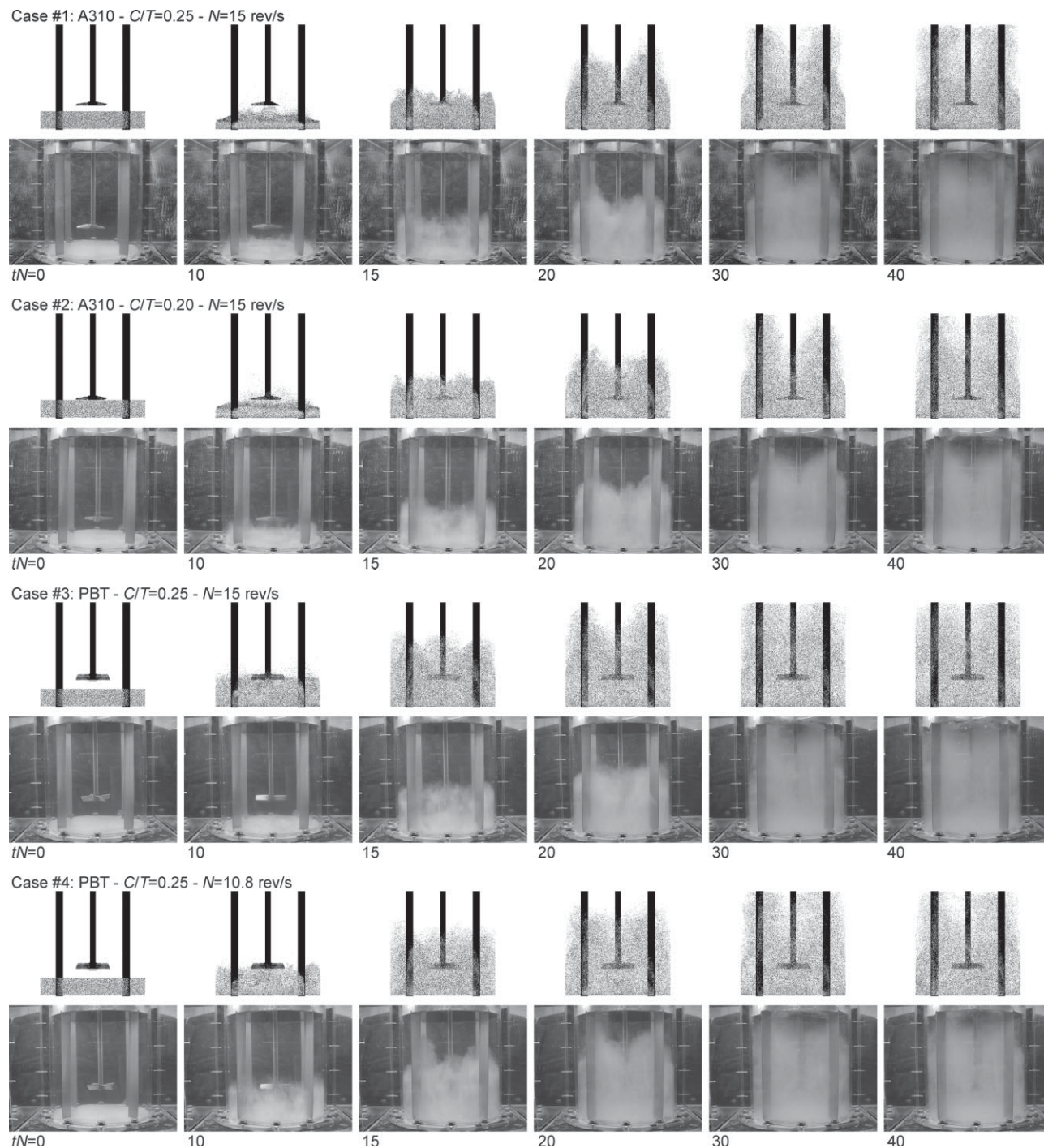


Figure 2. Side views for case #1 to #4 (top to bottom); simulation and experiments. Time from start-up increases from left to right and is given in the number of impeller revolutions.

Other features observed in the experiments are the sweeping of the bottom in the first 15 or so impeller revolutions with some solids remaining on the bottom underneath the impeller for a longer time. This patch of solids underneath the impeller is larger for the PBT cases compared to the A310 cases and is due to the A310 mainly pumping axially, while the stream coming from the PBT has a significant outward radial compo-

nent in addition to the axial component, see Fig. 6. The flow fields will be discussed in more detail in the next sub-section. This feature is picked up well in the simulations.

The random versus segregated initial condition in simulations and experiments, respectively, makes a direct comparison in terms of the evolution of the bronze particles impossible. However, it is possible to compare the fate in steady state of

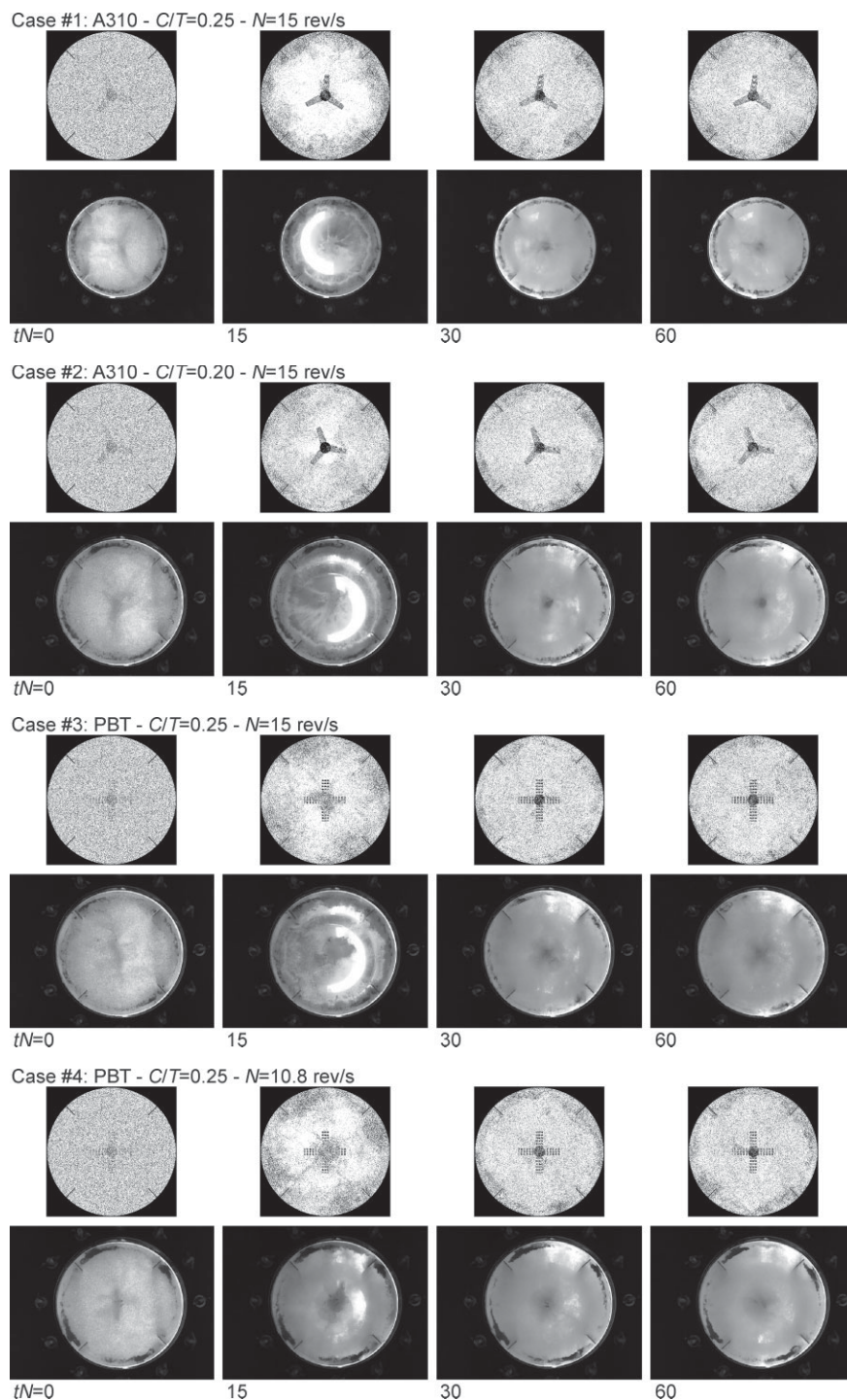


Figure 3. Views through the bottom of the tank for case #1 to #4 (top to bottom); simulation and experiments. Time from start-up increases from left to right and is given in the number of impeller revolutions. In this view, the impeller rotates counter-clockwise.

the bronze particles beyond $tN \approx 40$. The simulations do show a preferential concentration of bronze near the perimeter of the bottom, and the direction of rotation of the impeller is clearly visible in this respect with more bronze in front compared to in the wake of the baffles. Also, the effect of the

impeller speed is visible in the PBT simulations with more bronze detectable near the bottom for the lower speed, consistent with the experiment. The widths of the high-bronze regions are, however, overestimated by the simulations. This effect is likely due to limits in resolution and the one-way coupling modeling assumption: The resolution of the liquid flow is not sufficient to fully resolve the boundary layer above the bottom at the high Reynolds numbers. In addition, the liquid flow does not feel the presence of the particles and thus does not feel the bottom region getting rougher if many bronze particles are present there. In physical reality, this two-way coupling effect provides a feedback mechanism that localizes bronze at the perimeter of the bottom. For this reason, bronze concentrations in this region seem underestimated by the simulations. Limited resolution of the boundary layer and consequently overestimation of liquid fluctuations near the bottom makes the high-bronze region wider compared to the experiment.

In what follows, the results presented (Figs. 4 through 9) all relate to simulations. In Fig. 4, time series of the tank-average vertical particle location (per particle type, glass and bronze) as a function of time are given for case #1 to #4. In all cases, the start-up of the suspension process takes 20–30 impeller revolutions. Qualitative observations made in Fig. 2 for experiments as well as simulations are confirmed here: (1) Faster start-up for the PBT-driven flow compared to the A310; (2) a clear reduction in vertical (z) particle locations for the lower impeller speed of the PBT; (3) marginal effects of the A310 impeller clearance ($C/T = 0.25$ vs. 0.20). The time evolutions for glass particles and bronze particles are very similar. This is no surprise given that both sets of particles are dispersed in the same liquid flow field. On average, bronze is slightly lower in the tank than glass which is due to bronze's higher single-particle settling velocity U_{∞} .

For case #1, additional simulations regarding solids motion, not liquid flow, have been done. By default any particle can collide with any other. In the additional simulations, however, bronze can only collide with bronze, glass only with glass. It is as if there exist glass-only and bronze-only simulations. Given

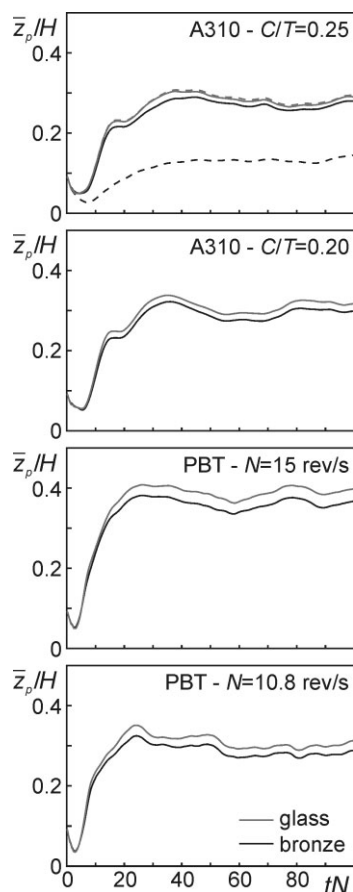


Figure 4. Time series of the average vertical location of glass and bronze particles for the four cases (top to bottom). The dashed curves in the upper panel are for particles that do not interact with the particles of the other type, i.e., bronze only collides with bronze, glass with glass.

the one-way liquid-solid coupling, however, all solids systems feel exactly the same liquid flow. The results of these variations to case #1 are presented in the upper panel of Fig. 4 as dashed curves. The absence of glass has profound impact for the distribution of bronze in the tank: the average vertical position of bronze is reduced by almost a factor of two. Apparently the collisions with the glass particles help suspend the bronze. The effect of bronze on glass is marginal (again, see Fig. 4, top panel). Note that the total mass of bronze is much less than the total mass of glass, i.e., by a factor of 20, and that the mass of a single glass sphere is much higher than that of a single bronze sphere, namely, by a factor of 10, so that collisions between glass and bronze do not significantly impact the glass particles. The observation of glass supporting bronze is consistent with experimental studies as reported by Ayranci and Kresta [8]. It should be reminded, however, that the present results are for dilute slurries. In [8], strong particle-particle interactions were observed for dense slurries. Our results show that these interactions exist even at low solids concentrations.

The way liquid, glass, and bronze interact in the default version of case #1, which includes glass-bronze collisions, is

further illustrated by the time series of kinetic energy and kinetic energy transfer rates illustrated in Fig. 5. The time series are recorded after a dynamically steady state has been reached. In steady state, the liquid provides the kinetic energy for the glass phase (overall $\Delta k/\Delta t > 0$ for liquid→glass), see the upper panel of Fig. 5. Also the glass→bronze transfer rates are positive, which means that bronze receives kinetic energy from the glass particles. That the bronze→glass rates are exactly the opposite of glass→bronze is a consequence of the fully elastic collision between all solid particles. Most of the energy bronze receives from glass is lost again to the liquid (liquid→bronze negative). There is, however, a net kinetic energy gain for the bronze. This eventually leads to a situation with a kinetic energy contained in the motion of the bronze particles that is a factor of 1.79 higher compared to the situation in which bronze does not feel the glass particles. In that latter situation bronze only receives energy from the liquid. The result of the higher energy is that the bronze particles get better suspended in the liquid and are able to reach, on average, higher positions in the tank, as witnessed in the upper panel of Fig. 4.

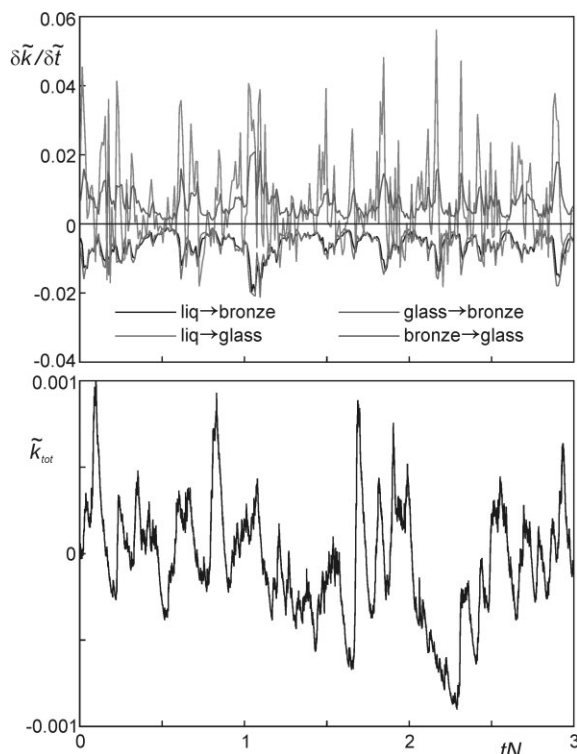


Figure 5. Time series of solids kinetic energy transfer (top) and total solids kinetic energy (bottom) over a steady time window of three impeller revolutions. $\frac{\delta \tilde{k}}{\delta t} \equiv \frac{\delta k}{\delta t} \frac{1}{N \frac{1}{2} \rho V_s v_{tip}^2}$ is the dimensionless kinetic energy being transferred from one phase to another phase (as indicated) per unit of time; V_s is the total solids volume (bronze plus glass) in the tank. $\tilde{k}_{tot} \equiv \frac{k_{tot} - k_{tot,0}}{\frac{1}{2} \rho V_s v_{tip}^2}$ is the dimensionless total solids kinetic energy relative to the energy at moment $t = 0$ of this time window. Case #1.

Data regarding collision frequencies support the above observations that particle dynamics is much affected by collisions. As an example, in case #1 and after steady state is reached, each particle collides on average almost five times with another particle per impeller revolution.

From the top panel of Fig. 5 it may seem that the sum of the various energy transfer rates is on average positive, which would mean that the solids are continuously gaining energy and the flow system is unsteady in the long term. To illustrate that this is not the case, in the lower panel a time series of the total kinetic energy of the solids in the tank is displayed. A strongly fluctuating signal is observed, but there is no systematic upward (or downward) trend.

4.2 Flow and Solids Concentration Fields

The results above, specifically those in Figs. 2 and 3 that compare experiments and simulations, provide some indication of the level of realism of the simulations. Specifically the overall suspension dynamics is represented well; the near bottom behavior requires higher resolution and a more complete representation of solid-liquid interaction physics. In what follows here, by means of the simulations the solids transport in the bulk of the tank and specifically the role of the baffles in moving the solids vertically is studied.

Fig. 6 presents the liquid flow patterns generated by the two impellers A310 and PBT. The impellers have the same diameter, revolve with the same angular velocity, and are located at approximately the same vertical position. Clearly the PBT creates a stronger flow and more turbulence, specifically in the upper regions of the tank. This is due to its higher power demand compared to the A310. The torque M to revolve the impeller is a direct outcome of the immersed boundary method to maintain no-slip on the impeller surface so that in the simulations the power can be determined as $P = 2\pi NM$. For the four cases as defined in Tab. 1, the simulations show power numbers of $Po = 0.34, 0.36, 1.40,$ and $1.41,$ respectively. The first two power numbers are for the A310 and show a weak effect of the impeller placement above the tank bottom with a 6% higher Po for the lower placement. The last two power numbers are for the PBT and indicate that Po is largely independent of Re . Literature values for the power numbers of A310 and PBT with $D = T/3$ are 0.3 and 1.3, respectively [14], where it should be noted that these are for an off-bottom placement of $C/T = 1/3$. Given our results, there is a weak effect of C/T on Po .

Also the direction of the stream emerging from the impellers is different, with a more vertical orientation for the A310. As described above, this generates flow underneath the impeller towards the bottom which helps in removing solids from that part of the bottom. The PBT has a more inclined, radially outward impeller stream and a relatively quiescent flow region underneath the impeller. This deposits solids at the center of the base where they remain for a relatively long time. Note that the impeller manufacturer recommends placing the A310 at $C/T > 0.35$ in solids suspension processes. With $C/T = 0.25$ and 0.20, as in the current case, non-ideal solids distributions are expected.

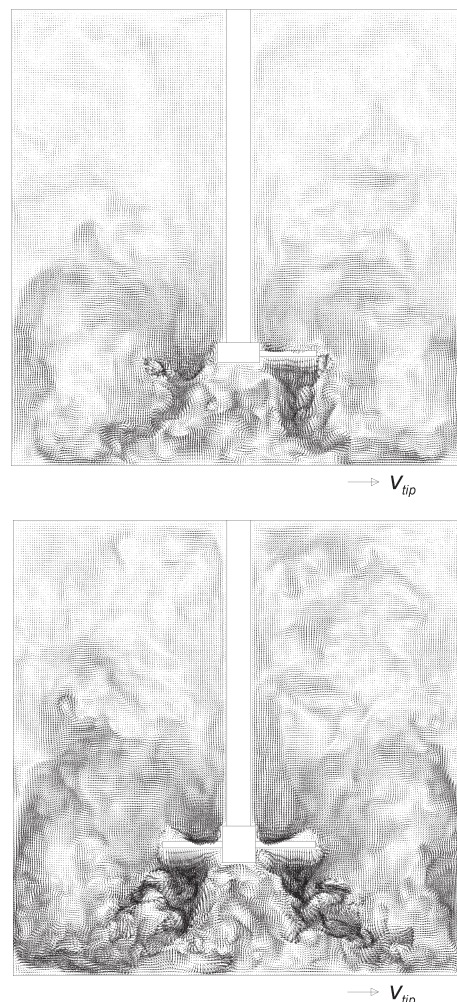


Figure 6. Snapshots of the liquid flow in a vertical cross section through the center of the tank and midway between baffles in terms of velocity vectors, 100 impeller revolutions after start-up. Top: case #1 (A310, $C/T = 0.25$, $N = 15 \text{ rev s}^{-1}$). Bottom: case #3 (PBT, $C/T = 0.25$, $N = 15 \text{ rev s}^{-1}$).

The way solids distribute throughout the tank is very different for the two impellers, as demonstrated in Fig. 7. The stronger turbulence with the PBT due to its higher power demand at the same rotation rate disperses the particles more uniformly through the tank, including its upper portions. As already anticipated by the time series (Fig. 4), bronze and glass behave similarly. With less bronze particles, their statistics, such as the average concentrations in Fig. 7, are noisier than those of glass. Despite this, it can be seen that the bronze particles reach a lower height in the tank compared to glass in the A310 case.

The interaction of particles with the impeller is very different for the two impeller types, see the panels in Fig. 7 at $z/T = 0.25$ (impeller level). The concentration fields shown are resolved for the impeller angle which means that one only adds to the average particle concentration field if the impeller is in the position as indicated in those panels. The streamlined, air-foil shape of the A310 makes a relatively smooth flow around

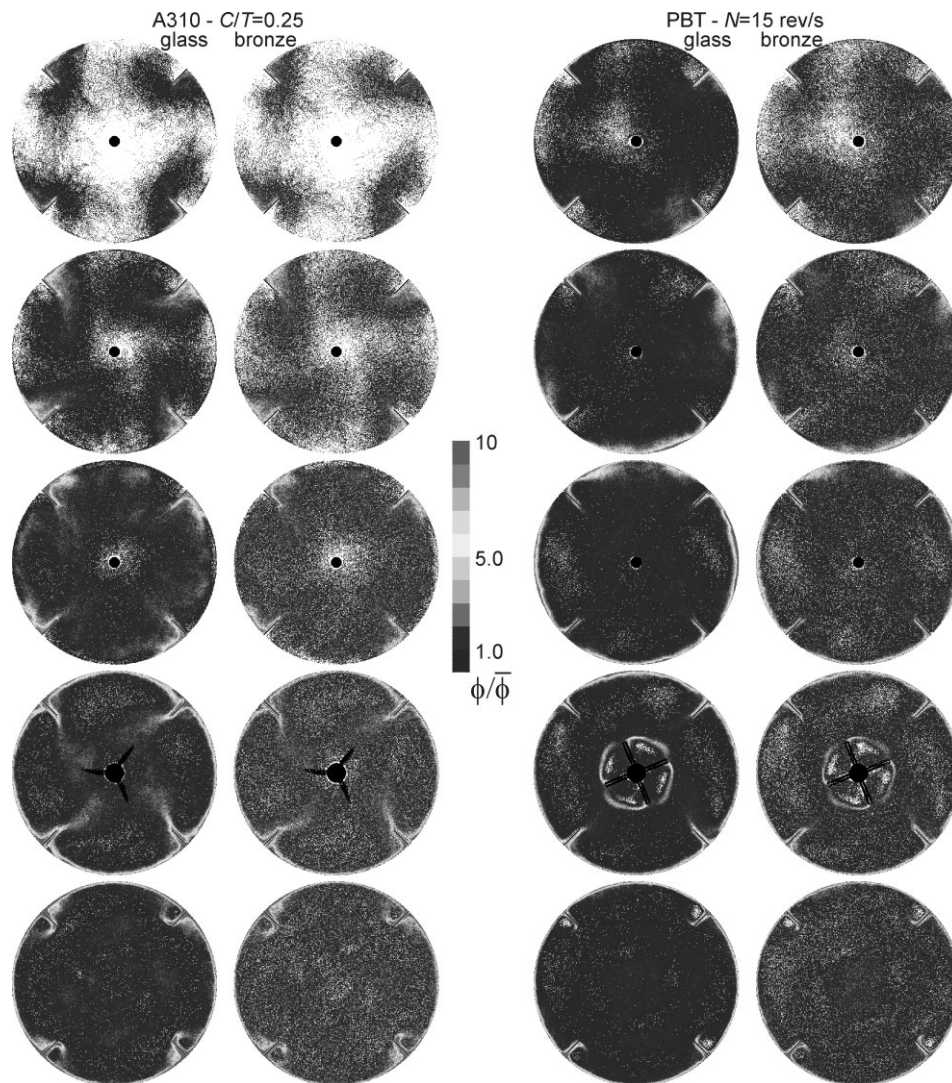


Figure 7. Solids (glass and bronze separately) concentrations in horizontal slices with thickness 0.017. Time averaging from $tN = 60$ to 100; impeller angle resolved data. Left: case #1, right: case #3. From bottom to top $z/T = 0.125, 0.25, 0.375, 0.5,$ and 0.75 . The tank-averaged volume fraction $\bar{\phi}$ is per particle type. White portions have not been visited by a glass or bronze particle during the averaging period. The impeller rotates counter-clockwise in this view.

the impeller and particles distribute quite uniformly there. The PBT on the other side creates pronounced structures, e.g., trailing vortices [24], in the liquid around it. Particles preferentially concentrate in the edges of the trailing vortices and stay away from the inner wakes of the blades.

The highest solids concentrations are found in front of the baffles, with “in front” defined based on the direction of impeller rotation. These high concentrations extend to high up in the tank since the baffles direct the flow in front of them in the upward direction. The vortex structures in the wakes behind the baffles are clearly visible through the concentration fields in the lower parts of the tank. The role of baffles in transporting particles up is further detailed in Figs. 8 and 9. The snapshots in Fig. 8 are of particles and particle velocities in vertical planes just in front and just behind two diametrically placed baffles. They visualize the on average upward solids

motion in front of the baffles and the (weak) downward motion behind them.

The inhomogeneous distribution of particles in the tank brought about by the A310 impeller is also apparent from Fig. 8. Solids concentrations along the wall and in the lower half of the tank are significant; the rest of the tank is largely void of solids. The more uniform dispersion of solids with the PBT comes at the price of higher power input. These observations cannot be made directly from the experimental side views since in these views the solids along the wall suggest their presence throughout the entire tank.

In Fig. 9, time series of the upward vertical volume flux of solids (glass plus bronze) through a cross-sectional area $w \times w$ in front of the baffles are presented. After a start-up phase with zero flux and then a spike with many particles passing through the $z = 0.375T$ monitor level, a dynamic steady state sets in.

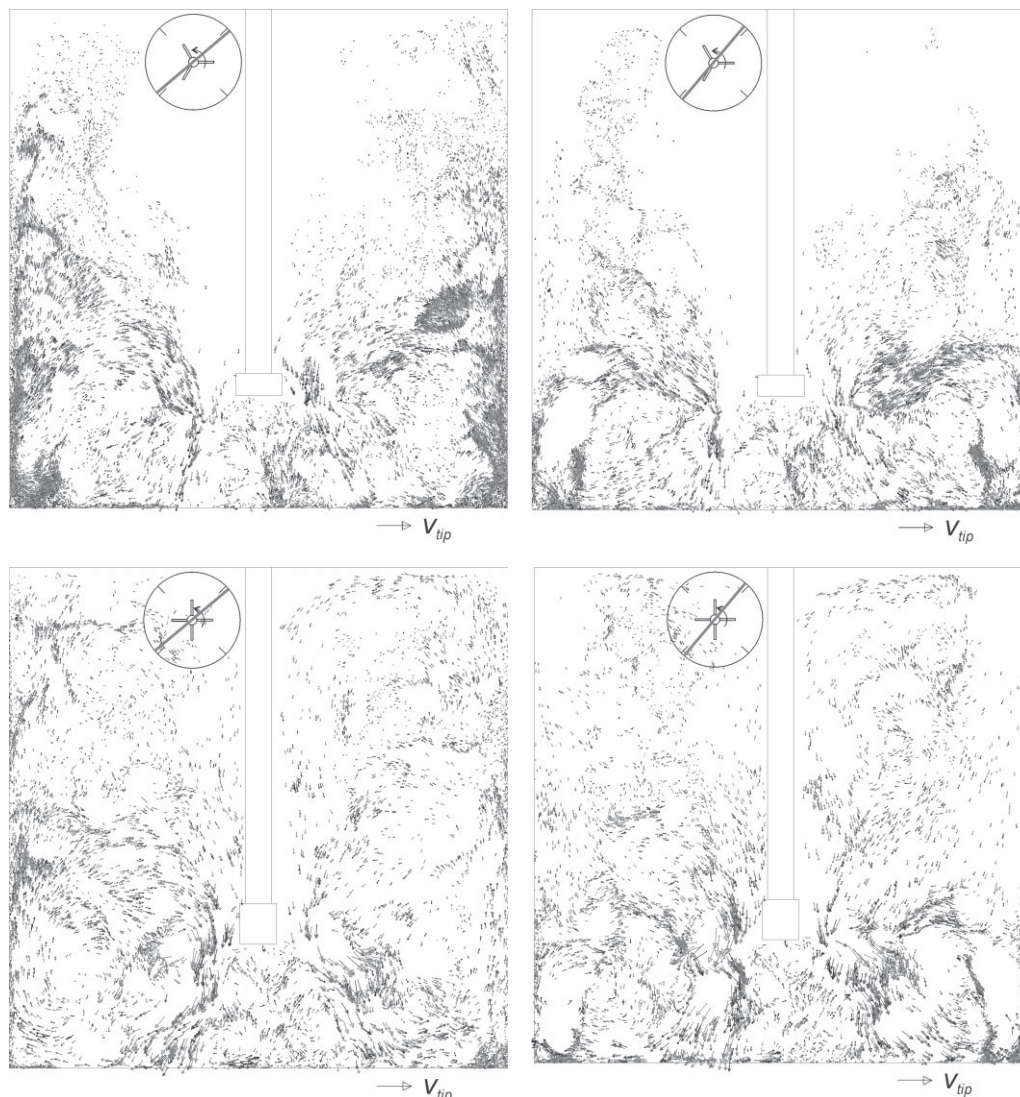


Figure 8. Snapshots. Particles and their velocity vectors in two vertical slices (thickness $0.01T$) through the center of the tank. Left: in front of the baffles; right: in the wake of the baffles. Top: A310, $C/T = 0.25$ (case #1); bottom: PBT, $N = 15 \text{ rev s}^{-1}$ (case #3).

Average solids fluxes for the PBT are much higher than for the A310 impeller. Note the different vertical scales in the time series for the A310 and PBT cases in Fig. 9.

The fluctuating parts of the vertical solids flux time series after steady state is reached have been analyzed in terms of their spectral characteristics in order to identify coherency/macro-instabilities [25–27]. In accordance with earlier results for A310 and PBT impellers with $D = T/3$ [26], no clear, dominant, low-frequency fluctuations could be identified. The peaks that appear for the first or second frequency point in some of the spectra in Fig. 9 relate to slow trends in the signals in combination with the limited length (70 impeller revolutions) of the time series of the spectra are based on, not to coherent motion. If macro-instabilities appear in turbulent stirred-tank flow, their frequencies are of the order of $fN = O(0.1)$ [26].

5 Summary and Conclusions

Experimental and computational visualizations of the start-up and subsequent steady state of a solids suspension process in a baffled mixing tank under strongly turbulent conditions were compared. Effects of impeller type, speed, and off-bottom clearance were investigated. The suspensions consisted of a bidisperse set of particles, glass and bronze. They both have a Stokes number of order one and a single-particle settling velocity of order 10^{-2} times the impeller tip speed. The solids volume fraction was 1 %, making this a dilute suspension. The latter allowed for simulations of an Eulerian-Lagrangian type where each particle was followed individually on its way through the tank. One-way coupling with solids feeling the liquid was assumed, the liquid not feeling the solids, justified by the dilute limit.

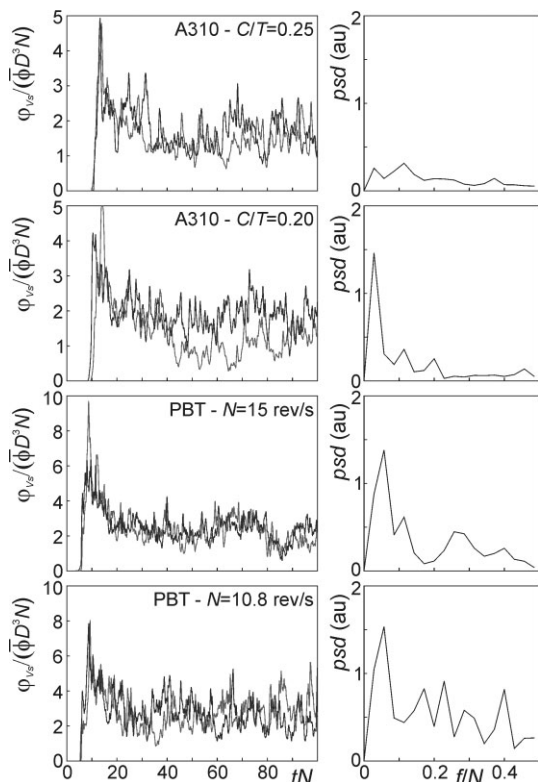


Figure 9. Left: time series of the vertical solids volume fluxes through a horizontal cross-sectional area $w \times w$ in front of two of the four baffles (the two curves are for two different baffles) at vertical location $z = 0.375T$. Right: power spectral density (psd) of the fluctuating (AC) part of the signals over the steady time interval $30 \leq tN \leq 100$. The spectra are based on volume flux time series in front of all four baffles.

The global start-up behavior of the suspension process was well represented by the simulations, including trends with regards to impeller type and speed. Some important details were not captured well by the simulations. They mainly related to what happens close to the bottom. These deviations were partly due to differences in initial conditions, partly due to a lack of resolution and the assumption that two-way coupling could be neglected in the simulations. Near the bottom, bronze and glass were to some extent segregated with bronze collecting near the perimeter of the bottom between the baffles. The simulations showed a much weaker segregation.

The simulations allowed for a detailed analysis of the suspension process. The direct relation between turbulence and solids distribution was demonstrated through comparison between an A310 impeller and a pitched-blade turbine, the latter having stronger turbulence due to its higher power number. Also the role of baffles in directing liquid flow and particles in the upward direction was highlighted. Interestingly, even under dilute conditions the interaction between the solid particles proved to be a significant factor in the suspension

process: in the absence of glass beads, the entrainment of bronze in the liquid was significantly less compared to the situation in which glass was present. It was demonstrated that this is the result of the glass providing most of the kinetic energy of the bronze particles through collisions. In the absence of glass, only liquid drag suspended the bronze particles and did so in a less effective manner.

The authors have declared no conflict of interest.

References

- [1] T. N. Zwietering, *Chem. Eng. Sci.* **1958**, 8, 244–253.
- [2] A. W. Nienow, *Chem. Eng. Sci.* **1968**, 23, 1453–1459.
- [3] G. Baldi, R. Conti, E. Alaria, *Chem. Eng. Sci.* **1978**, 33, 21–25.
- [4] J. T. Davies, *Chem. Eng. Process.* **1986**, 20, 175–181.
- [5] G. Montante, G. Micale, F. Magelli, A. Brucato, *Chem. Eng. Res. Des.* **2001**, 79, 1005–1010.
- [6] R. K. Dasari, R. E. Berson, *Chem. Eng. Technol.* **2011**, 34, 289–295.
- [7] G. Montante, F. Magelli, *Ind. Eng. Chem. Res.* **2007**, 46, 2885–2891.
- [8] I. Ayranci, S. M. Kresta, *Chem. Eng. Res. Des.* **2011**, 89, 1961–1971.
- [9] J. J. Derksen, *AIChE J.* **2012**, 58, 3266–3278.
- [10] J. J. Derksen, *AIChE J.* **2003**, 49, 2700–2714.
- [11] J. Smagorinsky, *Mon. Weather Rep.* **1963**, 91, 99–164.
- [12] R. Sungkorn, J. J. Derksen, *Phys. Fluids* **2012**, 24, 123303.
- [13] I. Ayranci, M. B. Machado, A. M. Madej, J. J. Derksen, D. S. Nobes, S. M. Kresta, *Chem. Eng. Sci.* **2012**, 79, 163–176.
- [14] D. Chapple, S. M. Kresta, A. Wall, A. Afacan, *Trans. IChemE.* **2002**, 80, 364–372.
- [15] L. Schiller, A. Naumann, *Ver. Deut. Ing. Z.* **1933**, 77, 318–320.
- [16] S. Succi, *The Lattice Boltzmann Equation for Fluid Dynamics and Beyond*, Clarendon Press, Oxford **2001**.
- [17] V. Eswaran, S. B. Pope, *Comput. Fluids* **1988**, 16, 257–278.
- [18] J. G. M. Eggels, *Int. J. Heat Fluid Flow* **1996**, 17, 307–323.
- [19] H. Hartmann, J. J. Derksen, C. Montavon, J. Pearson, I. S. Hamill, H. E. A. van den Akker, *Chem. Eng. Sci.* **2004**, 59, 2419–2432.
- [20] D. Goldstein, R. Handler, L. Sirovich, *J. Comput. Phys.* **1993**, 105, 354–366.
- [21] J. J. Derksen, H. E. A. van den Akker, *AIChE J.* **1999**, 45, 209–221.
- [22] J. J. Derksen, *Comput. Fluids* **2011**, 50, 35–45.
- [23] M. Chen, K. Kontomaris, J. B. McLaughlin, *Int. J. Multiphase Flow* **1998**, 24, 1079–1103.
- [24] J. J. Derksen, *Chem. Eng. Res. Des.* **2001**, 79, 824–830.
- [25] V. T. Roussinova, S. M. Kresta, R. Weetman, *Chem. Eng. Sci.* **2003**, 58, 2297–2311.
- [26] V. T. Roussinova, S. M. Kresta, R. Weetman, *AIChE J.* **2004**, 50, 2986–3005.
- [27] H. Hartmann, J. J. Derksen, H. E. A. van den Akker, *AIChE J.* **2004**, 50, 2383–2393.